Rotational Disorder in Twisted Bilayer Graphene

Thomas E. Beechem,[†,*] Taisuke Ohta,[†] Bogdan Diaconescu,[†] and Jeremy T. Robinson[‡]

[†]Sandia National Laboratories, Albuquerque, New Mexico, United States, and [‡]Naval Research Laboratory, Washington D.C., United States

ABSTRACT Conventional means of stacking two-dimensional (2D) crystals inevitably leads to imperfections. To examine the ramifications of these imperfections, rotational disorder and strain are quantified in twisted bilayer graphene (TBG) using a combination of Raman spectroscopic and low-energy electron diffraction imaging. The twist angle between TBG layers varies on the order of 2° within large (50−100 μm) single-crystalline grains, resulting in changes of the emergent Raman response by over an order of magnitude. Rotational disorder does not evolve continuously across the large grains but rather comes about by variations in the local twist angles between differing contiguous subgrains, ~1 μm in size, that themselves exhibit virtually no twist angle variation ($\Delta\Theta$ ~0.1°). Owing to weak out-of-plane van der Waals bonding between azimuthally rotated graphene layers, these subgrains evolve in conjunction with the 0.3% strain variation observed both within and between the atomic layers. Importantly, the emergent Raman response is altered, but not removed, by these extrinsic perturbations. Interlayer interactions are therefore resilient to strain and rotational disorder, a fact that gives promise to the prospect of designer 2D solid heterostructures created *via* transfer processes.

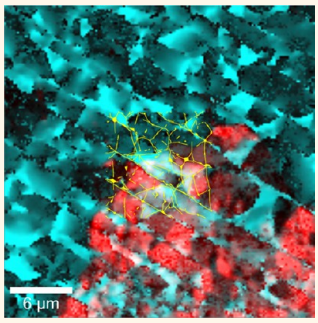

KEYWORDS: twisted bilayer graphene · interlayer coupling · rotational disorder · strain · Raman spectroscopy

Two-dimensional (2D) crystals are increasingly available in a variety of species,[1] as are methods of stacking these crystals to create complex hybrid solids of virtually any combination.[2−5] Interestingly, hybrid 2D crystals do not respond simply as the sum of the individual atomic layers but are differentiated by new properties that emerge from their interaction. For instance, interlayer interaction significantly enhances optical absorption in azimuthally rotated bilayer graphene (*i.e.*, twisted bilayer graphene (TBG))[6−8] and changes the electronic band structure of graphene when placed atop hexagonal boron nitride.[9−12] These emergent responses are not limited to graphene but are instead a general feature of stacked 2D crystals.[13] Factors modifying the interlayer interaction will therefore have large implications on the properties of solids built from atomically thin materials.

Azimuthal misalignment, or twist, acutely affects the interlayer interaction in 2D solids and, in particular, twisted bilayer graphene,[13,14] where it can significantly modify the material's electrical,[15] mechanical,[16,17] thermal,[18] and optical[6,7] properties. Realized when two graphene layers are rotated relative to one another, TBG possesses an electronic dispersion distinct from either that of mono- or bilayer graphene. Marked by a "monolayer-like" linear dispersion near the Dirac point combined with the appearance of low-energy van Hove singularities (vHs), the same features that differentiate TBG also depend upon the angle of twist, Θ.[14] Specifically, because of the twist, additional symmetry evolves in the form of a moiré superlattice.[14,19,20] The moiré superlattice imbues an extra periodicity that acts to impart a periodic potential.[13] This periodic potential, in turn, induces the band structure changes that are the specific hallmarks of TBG, as has been predicted extensively *via* theoretical approaches[14,15,19,21−27] and observed experimentally with scanning tunneling microscopy (STM),[10,28] angle-resolved photoemission spectroscopy (ARPES),[13] or Raman spectroscopy.[29−31] Driving the distinguishing aspects of TBG, therefore, is this periodic potential and the twist-angle-dependent periodicity of the moiré that effectively acts to apply it. Twist angle variation, whether intentional or not, will then directly impact the dispersion and hence the properties of the material.

Layered 2D materials have a proclivity toward rotational disorder. Unlike conventional

* Address correspondence to tebeech@sandia.gov.

Received for review November 20, 2013 and accepted January 24, 2014.

Published online January 24, 2014
10.1021/nn405999z

thin films where strong chemical bonds exist out of the atomic plane, van der Waals (vdW) forces in 2D crystals are insufficient to strongly lock the layers into a particular atomic registry. The individual atomic planes are thus capable of sliding or rotating relative to one another without a preferred orientation.[32] Any one of several effects could therefore induce rotations within and between the layers including strain,[33] the transfer process, or the synthesis of the atomic planes themselves.[34,35] For this reason, we examine the introduction, magnitude, and ramifications of rotational disorder on the emergent properties of TBG prepared *via* layer transfer. Using a combination of Raman spectroscopic imaging and area-selective low-energy electron diffraction (LEED) mapping, rotational disorder is shown to (1) be comparatively small, <2°, within a nominally "uniform" grain, (2) significantly alter, but not remove, the resonant Raman response, and (3) evolve in a stepwise fashion through the formation of contiguous subgrains approximately 1 μm in size having uniform Raman intensity that themselves form in conjunction with the large strain variations that exist both within and between the atomic layers. Taken together, the results indicate the resilience of the long-range interlayer interaction generated by the moiré superlattice and point to the promise of robust designer hybrid 2D crystals.

RESULTS AND DISCUSSION

Twisted bilayer graphene was fabricated by transferring a monolayer of chemical vapor deposited (CVD) graphene grown on copper,[36] hereafter referred to as the overlayer, onto a quasi-freestanding epitaxial monolayer of graphene grown on the (0001) face of silicon carbide (SiC),[31] denoted as the underlayer. Further details regarding the fabrication of TBG can be found in the Methods section. The resulting polycrystalline film is composed of TBG having numerous grains of ~50−100 μm each with differing twist angle. As the epitaxial graphene has a single crystallographic orientation, TBG grains are defined by single lobes of the graphene islands that nucleate with variable orientation during CVD synthesis.[31,34] The combination of a CVD-derived overlayer and epitaxial underlayer is particularly suited to study the effects of rotational disorder and strain. In particular, epitaxial graphene grows with strain[37,38] apart from rotational disorder, while CVD-synthesized graphene exhibits rotational disorder[34,35] but is nearly strain free.

Figure 1a provides a representative Raman image 30 × 30 μm in size acquired with 532 nm light that includes two separate grains of varying twist angle. For the grain in the upper portion of Figure 1a, the G-mode (~1600 cm^{-1}) intensity is similar to that of Bernal stacked bilayer graphene, while the 2D (G′)-mode (~2700 cm^{-1}) is well described by a "monolayer-like" single Lorentzian function having a width of less than 25 cm^{-1} (see spectrum N1 in Figure 1c). Given the probe wavelength of 532 nm, these spectral characteristics indicate a twist angle of >15° for this grain.[39−41] Unique identification of the twist angle is not possible, however, due to the effects of strain and carrier concentration on the Raman spectrum, as is addressed subsequently. For easy differentiation, we term this the nonresonant grain.

A much stronger G-mode intensity (~1600 cm^{-1}) is observed for the grain in the lower right-hand corner of Figure 1a, increasing by as much as 35× relative to that of monolayer graphene. For the same location on the sample, this large response is not seen when utilizing a 785 nm laser (see inset of Figure 1a). We therefore term this the resonant grain. The large magnitude of the G-mode response and its wavelength dependence are a consequence of the electronic dispersion of TBG where efficient pathways for light absorption are created and constructive interference of the G-mode Raman scattering processes[39,42] occurs due to the emergence of vHs.[8,30,40,41,43] Since the van Hove singularities move relative to the Dirac point as a function of rotation angle, the processes of light absorption necessary to induce a resonant Raman enhancement of the G-mode are dependent upon the twist angle. Therefore, a TBG grain resonant under one excitation energy will not be resonant at another. From an experimental standpoint, the Raman signal is enhanced when the energy of the incoming laser is comparable to the energetic separation of the low-energy vHs and is maximized when the energies are equivalent. When interrogating with 532 nm radiation, this resonance occurs for a critical angle of $\Theta_c \approx 12.5°$.[6,39] For rotations away from this critical angle, the G-mode intensity varies as a Lorentzian function, as discussed later.[39]

Beyond the observation of resonant and non-resonant responses in this region, we note two additional features in the Raman data. First, although resonance is observed over the entirety of the resonant grain, the intensity of the G-mode fluctuates by as much as a factor of 10 within this area (compare spectra R1 and R2 in Figure 1c). The histogram in Figure 1b reveals the extent of these variations. Second, peak splitting of the Raman modes occurs intermittently over the entirety of the examined region regardless of grain (compare spectra R3 and N2 of Figure 1d). This splitting indicates that the under- and overlayer are unequally affected by perturbations that modify the Raman response, such as strain and carrier concentration.[44,45] Notably, since the G-mode resonance remains in spite of the splitting (see spectrum R3 in Figure 1d), TBG retains its interlayer coupling even in the presence of these perturbations. Subsequently, we show that the G-mode intensity variations are a consequence of the rotational disorder, while the spectral splitting arises from inequivalent straining of the under- and overlayer.

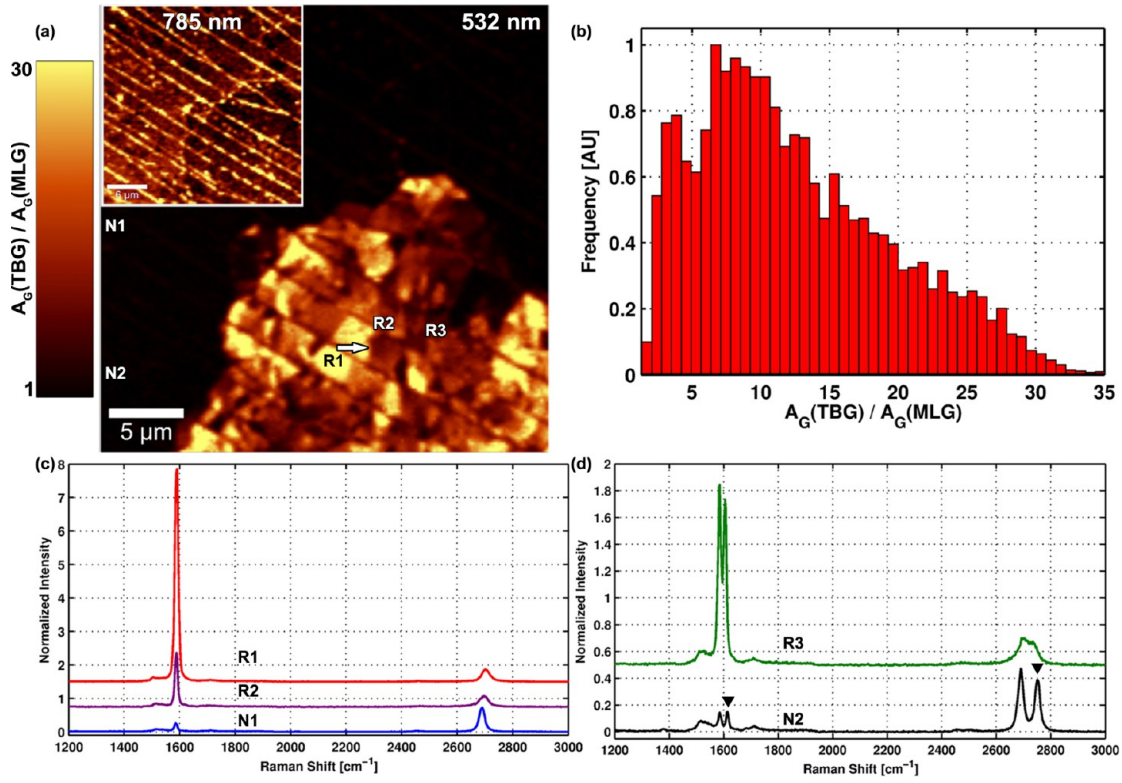

Figure 1. (a) Raman G-mode intensity normalized relative to the intensity of a monolayer graphene acquired using 532 nm incident radiation. Enhancement of the Raman signal is observed within a large grain in the lower right-hand corner termed the resonant grain. (Inset) The same area probed with 785 nm light where the intensity over both grains is comparable to Bernal stacked bilayer graphene. (b) Histogram of the G-mode intensity within the resonant grain. (c and d) Representative spectra (532 nm) acquired within both the resonant (R) and nonresonant (N) grains acquired at locations denoted by the labels in (a). Spectra are normalized relative to the strength of the second-order band of SiC at 1850 cm^{-1}.

To better understand the variable Raman intensity response within the resonant grain, variations in the G-mode intensity were compared to AFM-derived topography of the same resonant and nonresonant grains analyzed in Figure 1. Figure 2 shows that wrinkles and blisters are observed over the entirety of the sampled region regardless of the grain.[6,46] These features are attributed to residual debris present on each graphene surface at the time of transfer, which eventually coalesce to form the wrinkles and blisters observed here and reported previously.[5,46] Not surprisingly, where the wrinkles or blisters are present, the resonant Raman response is removed since interlayer separations of more than ~1 Å decouple the layers.[39] We also observe that the shape of the wrinkles and blisters qualitatively match the boundaries of "subgrains" that exhibit a more uniform Raman intensity response (see arrows in Figure 2 inset). Since even a few angstrom shift in one layer of TBG can change the local stacking sequence, the distortion induced by wrinkling and bubbling most likely induces variations in the local twist angle between the subgrains that are defined by these features, as discussed in detail later.

The presence and magnitude of local rotational disorder was further examined using LEED mapping. LEED mapping quantifies the twist angle between the over- and underlayer using the relative orientation of each layers' first-order diffraction spots and thus provides a direct probe of azimuthal deviations. Angle determination is accomplished by first quantifying the intensity of the LEED image about an arc that intersects each of the layers' first-order diffraction spots (see Figure 3a). The relative orientation of the layers is specified by fitting the intensity profile about the arc (red dotted line in Figure 3a) and then comparing the angles of the resulting intensity maxima (Figure 3e).

Figure 3 shows the results from a two-dimensional LEED map of the TBG sample examined in Figure 1 and Figure 2, though acquired at a different location on the sample. The map was acquired by translating the electron beam (0.5 μm diameter) over a 100 $\times$ 40 μm area while acquiring a diffraction pattern every 2 μm. Figure 3b–d provides histograms of the orientations of the (b) underlayer and (c) overlayer along with (d) the extracted twist angle of a single TBG grain. Below each histogram is the corresponding LEED map of the orientations' spatial distribution (Figure 3f–h). Angular variation in the local orientation is larger for the overlayer as compared to the underlayer. While the angular deviation of the underlayer (0.7° fwhm, Figure 3b) is on par with the experimental uncertainty of the LEED

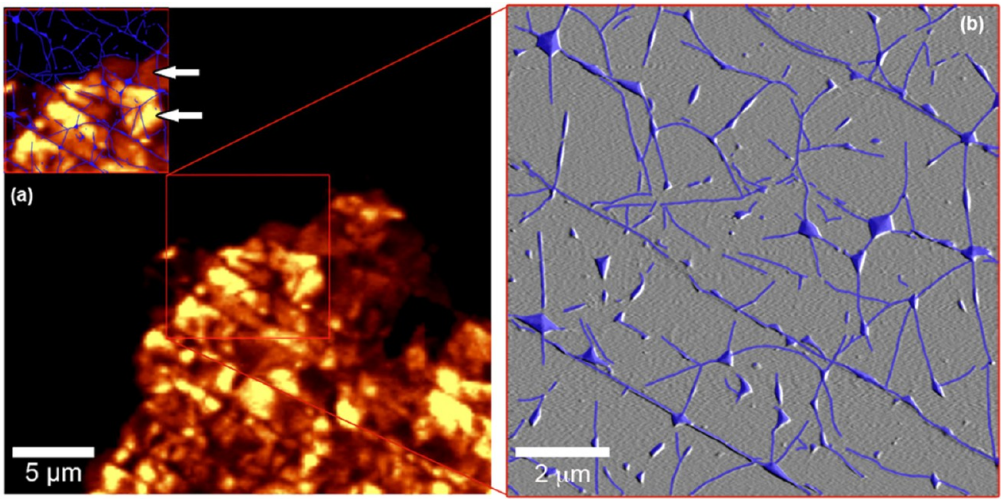

Figure 2. (a) G-mode intensity with red box indicating region of AFM analysis. (Note: Raw intensity image is provided here to enhance contrast.) (b) AFM false color image (derivative of topography) including both the resonant and nonresonant grains in (a). Inset: AFM image overlaid atop intensity image.

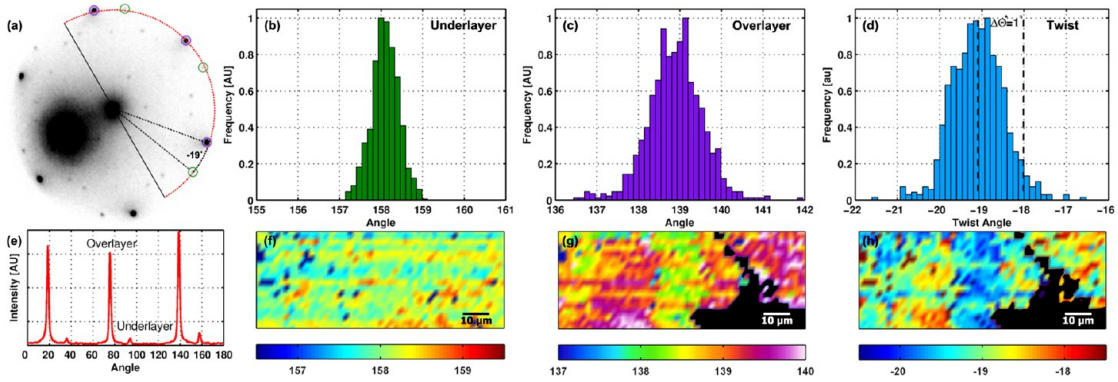

Figure 3. (a) LEED pattern of TBG exhibiting a twist angle of −19°. First-order diffraction spots of the underlayer and overlayer are highlighted by the green and purple circles, respectively. Quantification of the orientations occurs through analysis of the intensity profile (e) along an arc (red dotted line) encompassing these spots. Orientations of the (b) underlayer and (c) overlayer orientation along with the resulting (d) twist angles are shown *via* (b−d) histograms and (f−h) maps of their spatial distributions. The black regions within the overlayer and twist angle maps correspond to a separate grain having a different orientation.

measurement, the accompanying spread in the overlayer orientation is over a factor of 2 larger (1.4° fwhm, Figure 3c). The resulting extracted twist angle variation (Figure 3d) is consequently determined by the overlayer. We also point out the subtle structure in the twist angle map (Figure 3h) that is qualitatively similar in size and shape to the subgrains discussed earlier. All together, the LEED results indicate that (1) rotational disorder on the order of up to ∼2° exists within single grains (Figure 3d) and that (2) this disorder is driven primarily by variations within the overlayer.

To examine whether the intensity variations of the resonant grain observed in Figure 1a are due to the rotational disorder observed in Figure 3d or separate extrinsic factors such as strain or doping, we convert the normalized G-mode intensity ($A_{G,TBG}/A_{G,MLG}$) to an equivalent angle and compare the results to the measured variation in twist angle using LEED. $A_{G,TBG}/A_{G,MLG}$ is known to follow a Lorentzian dependence as a function of twist angle given by[39]

$$\frac{A_{G,\,TBG}}{A_{G,\,MLG}}(\Delta\Theta) = \alpha\frac{\gamma^2}{(\Delta\Theta^2+\gamma^2)} \qquad (1)$$

where $\Delta\Theta = |\Theta - \Theta_c|$ is the absolute difference of the twist angle from the critical angle we term the relative twist angle, α is a scaling factor assumed to be the intensity at the critical angle, and γ is the half-width at half-maximum taken to be 0.85° for 532 nm light.[39] Using eq 1, the normalized G-mode intensity distribution (Figure 1b) is converted to a twist angle distribution within the resonant grain. The resulting histogram is shown in Figure 4a, where the greater than 30-fold differences in the G-mode intensity correspond to rotational disorder having a magnitude of only 2°. Additionally, we find that the average twist angle of the resonant grain is ∼1° away from the critical angle. Because of the symmetry of the Lorentz function, however, use of the G-mode intensity provides only

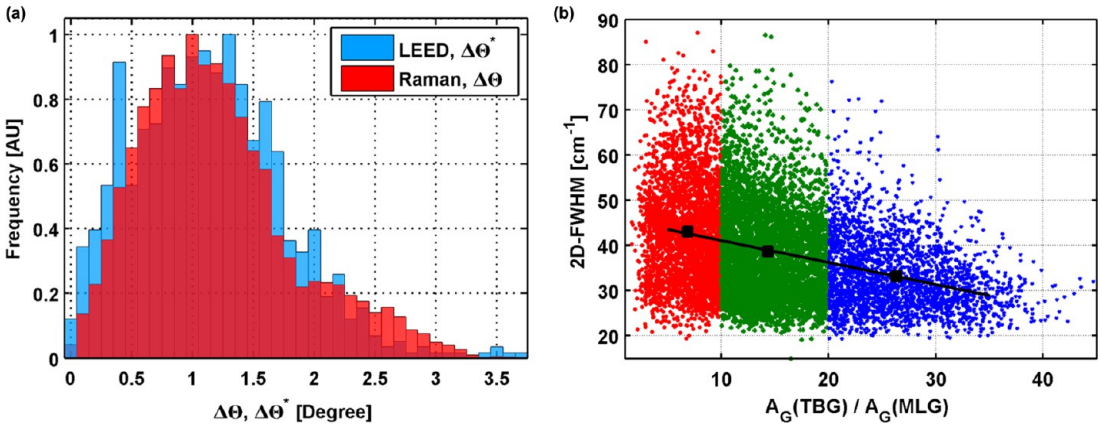

Figure 4. (a) Comparison of rotational disorder derived from Raman spectroscopy and LEED analysis. The Raman-based histogram is plotted as a function of magnitude away from the critical angle, $\Theta_c = 12.5°$. LEED data are referenced to an angle of $\Theta_c^* = -18°$ denoted by the dashed line in Figure 3d. (b) 2D-mode fwhm *versus* relative G-mode intensity where colors are utilized to highlight three different ranges. The larger black markers correspond to the mean values within each color where a fitted line to these values is utilized as a guide to the eye.

the magnitude away from the critical angle rather than the twist angle itself.

For this reason, the 2D-mode fwhm is also utilized in order to determine whether the average twist angle of the entire resonant grain is larger, or smaller, than the critical angle, $\Theta_c = 12.5°$.[41] Ideally, variations in the 2D-mode's peak position and fwhm could augment the intensity information to definitively stipulate the twist angle on a per pixel basis.[41] However, due to the finite spectral resolution of the Raman system, the small twist angle variation, and the complicating presence of strain, twist angle determination was possible only in an average sense over the entire resonant grain. Figure 4b compares the 2D-mode fwhm to the normalized G-mode intensity where on average the 2D-mode fwhm trends with negative slope. Since increases in the G-mode intensity correspond to angles closer to Θ_c, the negative trend indicates that pixels having an angle nearer to Θ_c have a smaller 2D-fwhm than those further away. For angles close to the critical angle ($\Delta\Theta < 4°$), theory[41] and experiment[39,40] have shown that the 2D-mode fwhm decreases with increasing twist angle. Taken together, this implies that pixels further from Θ_c (*i.e.*, those pixels with smaller G-mode intensity) have a twist angle, Θ, less than those closer to the critical angle since their 2D-fwhm is larger. By extension, the resonant grain has, therefore, an average twist angle less than Θ_c. When combined with information obtained from the G-mode intensity, this allows us to specify that the nominal twist angle of the entire resonant grain is 11.5°.

Owing to the fact that only the magnitude away from the critical angle can be determined on a per pixel basis from eq 1, the LEED-derived twist angle histogram (Figure 3d) was recast in order to compare with the Raman measurements. This was accomplished by transforming every LEED measured twist angle, Θ, into an absolute difference from an angle, Θ_c^*, *via* the relation $\Delta\Theta^* = |\Theta - \Theta_c^*|$. We define $\Theta_c^* = \mu + \delta$ where $\mu = 19°$ is the mean twist angle of the grain probed in Figure 3d and $\delta = 1.1°$ is the mean value of the Raman distribution given in Figure 4a. Similar results are arrived at if δ is chosen to be $-1.1°$. This choice of δ ensures that the center of the LEED distribution will lie at $\sim 1°$ like that of the Raman distribution, thereby allowing for comparison of the angular variation about this point. Overlaid atop one another in Figure 4a, the variations in angle between the Raman- and LEED-based measurements are very similar. As LEED measures the angle directly, this similarity supports the deduction that variations in the Raman intensity are due to rotational disorder.

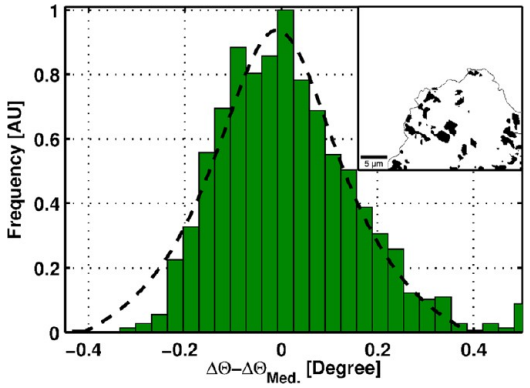

Figure 5. Histogram of variations away from the median twist angle for selected subgrains aggregated for all the black regions identified within the inset. Dotted line in inset defines the boundary of the resonant grain.

Rotational disorder does not evolve in a continuous manner across large-area grains. Rather, we find individual subgrains have virtually no measurable disorder within them but are rotated relative to one another. To gain sufficient statistical certainty to make this claim, we select a number of subgrains (inset of Figure 5) that have a nominal twist angle within 0.4° of

Θ_c and quantify the difference between the relative twist angle of an individual pixel, $\Delta\Theta$, to the median relative twist angle, $\Delta\Theta_{Med.}$, for that particular subgrain. The median relative twist angle is defined as the median of all relative twist angles for an individual subgrain. As shown in Figure 5, rotational disorder within individual subgrains is on the order of only 0.17° (fwhm), a value that is on par with the uncertainty of the Raman measurement. Near constancy of the twist angle is consistent with observations of uniform stacking between two graphene layers that has been shown to persist over 100's of nanometers.[39,47] Like the solitons observed by Alden *et al.*,[47] the size of these regions is limited by disorder and wrinkling, as shown in Figure 2.

It is known that local strain variations can be relaxed through wrinkling within a graphene layer.[48,49] In the TBG samples studied here, there is a measurable difference in strain state between the epitaxial graphene underlayer (>0.3% compressive strain) and transferred CVD graphene overlayer (<0.05% compressive strain). Additionally, AFM (Figure 2b) and Raman (Figure 5) measurements suggest that wrinkles in the overlayer define the boundaries of subgrains with relatively uniform rotation. To further investigate the relation between strain, wrinkling, and subgrains, we extract both strain and carrier concentration in each layer through analysis of the G- and 2D-mode peak positions.[38,50] In short, each acquired spectrum was fit to the sum of two Raman spectra of graphene—one for the overlayer and one for the underlayer—to account for the observed splitting of the modes (see Figure 1d). Linewidths (fwhm) were assumed to be identical for each of the layers but allowed to vary for each separately acquired total spectrum. Additionally, the second-order SiC signal was fit to ensure accuracy in the determination of the G-mode peak position. Results were grouped and assigned to a respective layer by assuming that, of the two fitted peak positions for a given mode, the one having the largest Raman shift was associated with the underlayer (see peaks denoted by triangles in spectrum N2 of Figure 1d).

Strain and carrier concentration are quantified by assuming that the total shift in the G- and 2D-modes peak positions is due to the superposition of the effects of strain and carrier concentration according to

$$\Delta\omega_{i,k} = \sum_{i,k}^{2}(\Delta\omega^{\varepsilon}_{i,k} + \Delta w^{e}_{i,k}) \qquad (2)$$

where $\Delta\omega^{\varepsilon}_{i,k}$ is the shift of the kth mode (G or 2D) away from its relaxed value of ω^{o}_{k} due to strain in the ith layer and $\Delta\omega^{e}_{i,k}$ is the change due to doping. For TBG, the peak position of the G-mode is insensitive to twist angle, allowing us to utilize the relaxed value of monolayer graphene, $\omega^{o}_{G} = 1582\ cm^{-1}$.[18,39,41] The peak position of the 2D-mode, in contrast, is highly sensitive to twist angle and blue-shifts relative to the relaxed monolayer value of $\omega^{o}_{MLG} = 2677\ cm^{-1}$ due to band structure alterations irrespective of the presence of strain and carrier concentration. For large twist angles like that of the nonresonant grain Figure 1a, the magnitude of the twist angle induced shift, denoted $\Delta\omega_{TBG}$, is 6 cm^{-1} under 532 nm illumination. Near resonance, the magnitude of the shift is much larger, reaching 15 cm^{-1}.[39−41] To calculate the strain and carrier concentration, changes in the 2D peak positions are thus quantified relative to these twist-induced alterations. That is, $\omega^{o}_{2D} = \omega^{o}_{MLG} + \Delta\omega_{TBG}$, where $\Delta\omega_{TBG}$ is 6 or 15 cm^{-1} for the nonresonant and resonant grain, respectively.

The strain contribution is estimated using the Gruneisen parameters *via*

$$\Delta\omega^{\varepsilon}_{i,k} = -2\gamma_k\omega^{o}_{k}\varepsilon_i \qquad (3)$$

where γ_k is the mode-dependent Gruneisen parameter and ε is the strain. We assume Gruneisen parameters of monolayer graphene corresponding to 2 and 2.8 for the G- and 2D-mode, respectively.[45] Previous theoretical predictions of the TBG Raman response have similarly presumed that the phonon behavior is similar to that of monolayer, in line with this assumption.[41,51] An empirical relationship linking the shift of each mode with the carrier concentration[44] is utilized to quantify the doping contribution, $\Delta\omega^{e}_{i,k}$, which is assumed to be p-type based on previous ARPES results of the same sample.[13] Finally, eq 2 is solved for each of the modes simultaneously allowing for the specification of both strain and carrier concentration within each layer. On the basis of this procedure, we estimate the difference in Fermi energies between the two layers to be 57 meV, a value similar to that measured on the same sample using ARPES.[13]

The resulting images of the strain distribution across the surface for both the under- and overlayer are shown in Figure 6a and b, respectively. Note that this is the same location of the sample as that of Figure 1. Identification of the underlayer is based upon similarities in the magnitude and morphology of the strain to that of the original epitaxial monolayer before transfer (Figure 6c inset). Measurable differences in the magnitude of strain evolve between the two layers. In certain locations, for example, strain in the underlayer exceeds that of the overlayer by more than a factor of 3. Effectively, the layers are to some extent mechanically separate despite being, from an electronic perspective, highly interacting owing to the persistence of the G-mode resonance that is observed.

Complete transmission of strain between the layers does not occur because of both weak out-of-plane van der Waals bonding and the azimuthal misalignment of the graphene planes. Twisting two graphene layers relative to one another reduces the adhesion energy between them[16] and can give rise to superlubricity.[52−57] To transmit strain, however, strain energy "lost" to

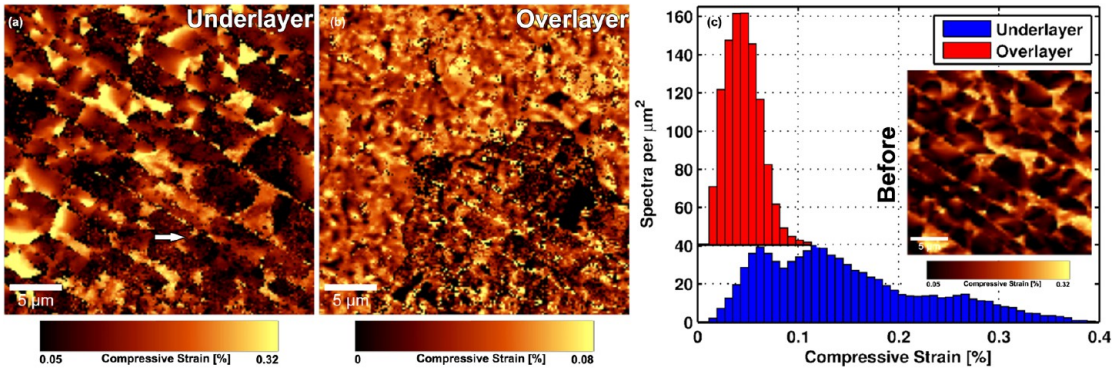

Figure 6. Strain distribution within the (a) underlayer and (b) overlayer along with a (c) histogram of these images. The inset of (c) shows the strain distribution of this same sample before transfer. Note: Color scales are different for the under- and overlayer in order to highlight variations across the respective surfaces.

deforming the two graphene lattices must be balanced by a "gain" in their adhesion energy. In this case, the adhesion energy to be gained is minimal, and so the layers remain, to first order, mechanically independent. Mechanical independence accompanied by significant electronic interaction is a unique feature of 2D crystals and, in contrast to other methods of thin-film synthesis (*e.g.*, physical vapor deposition, epitaxy) allows materials with very different lattice constants to be combined without the development of large strains. It should not be concluded, however, that strain is incapable of impacting the band structure of 2D crystals and, in particular, TBG. Rather, for the magnitude observed here (*i.e.*, a maximum compressive strain of ~0.4%), its impact is small. This is consistent with theory where a ~0.4% strain alters the energies of the van Hove singularities relative to the Dirac points by less than 1.5%,[58] whereas a 1° rotation alters these energies by ~10%.[8]

Finally, to explore correlations among strain, wrinkles defining the boundaries of the subgrains, and rotational disorder, Figure 7 shows a composite image of (i) the underlayer strain distribution of Figure 6a overlaid atop, (ii) the G-mode intensity of Figure 1a accompanied by the (iii) thresholded AFM topography of Figure 2b. We first note that the magnitude of the strain is not directly correlated to regions of either higher or lower Raman intensity (see horizontal arrow in Figure 7, Figure 6a, and Figure 1a), where relatively uniform amounts of strain separate regions of high and low Raman response. Thus, the magnitude of strain is not directly correlated to the rotational disorder.

Strain gradients, on the other hand, do seem to be associated with rotational disorder. Specifically, regions having a large strain gradient frequently correlate to boundaries separating adjacent subgrains with very different G-mode intensities (see vertical arrow in Figure 7) and hence twist angle. Oftentimes, topographical wrinkles are co-located with these boundaries as well. In light of these observations, we reiterate that wrinkles form, at least in part, as a consequence of interlayer contaminants that coalesce in response to

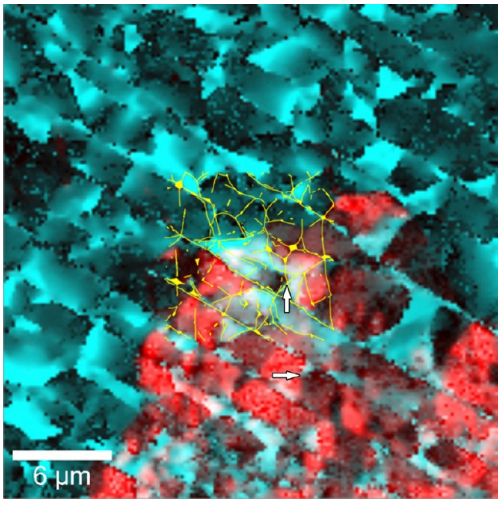

Figure 7. Composite image of the thresholded AFM topography (yellow), underlayer strain distribution (blue), and the G-mode intensity (red). For the strain (blue) and G-mode intensity (red), brighter colors correspond to larger magnitudes. Quantitative values are given in the scale bars of Figure 6a and Figure 1a for the strain and G-mode intensity, respectively.

being squeezed by the van der Waals forces between each graphene layer.[5,46] Agglomeration of the contaminants will occur, therefore, in regions of lowest interlayer interaction. In regions of high strain gradient, meanwhile, the periodicity of the moiré is locally disrupted, leading to a reduction of the interlayer interaction. Wrinkles will therefore preferentially form in these local minima of interlayer interaction that arise due to the strain gradients. From the standpoint of rotational disorder, the mechanical deformation caused by wrinkling induces the overlayer to rotate owing to the minimal amount of energy required to move in such a way.[33,57] Rotation, in turn, causes alterations in the band structure and thus the emergent response of the material, as evidenced by the changes in the G-mode intensity. Since the strain variations and wrinkling occur on a length scale of 1 μm, subgrains with near constant twist angle are observed

only on these length scales even as the grain itself has a size nearly 2 orders of magnitude larger.

CONCLUSION

The presence of rotational disorder within stacked twisted bilayer graphene has been investigated using a combination of Raman and LEED imaging. A single TBG grain was observed to vary in its twist angle by ~2°, which in turn induced variations of over 30 in the resulting emergent Raman response. The rotational disorder is correlated to strain variations and wrinkling across the surface. These wrinkles cause rotation between discrete subgrains that themselves have nearly constant twisting angle. In spite of these effects, the emergent Raman response persists. Taken together, these results demonstrate the robustness of 2D crystals to imperfection and point to the promise of designer hybrid solids created *via* layer transfer.

METHODS

Twisted bilayer graphene was realized by transferring a monolayer of CVD-derived graphene onto a monolayer of epitaxially grown graphene. Synthesis of the CVD-based overlayer and the epitaxial underlayer was accomplished using established methodologies.[6,31,36,59] Transfer of the overlayer onto the underlayer took place using previously reported processes by which poly(methyl methacrylate) (PMMA) stabilizes the CVD-derived graphene (*i.e.*, the overlayer) as the underlying copper is first removed.[36] The PMMA/CVD graphene stack is then transferred onto the epitaxial underlayer, and the PMMA support film is eliminated using acetone.[6,31] Low-energy electron microscopy is utilized to confirm that the transfer results in bilayer graphene.[31,60]

Raman spectroscopic measurements were performed with a WiTec Alpha300R Raman imaging system using a 100×/0.9 NA objective, resulting in beam diameters of ~500 nm when utilizing the 532 nm laser and less than 1 μm for 785 nm. Spectra were acquired every 180 and 300 nm for the 532 and 785 nm cases, respectively. A 600 l/mm grating combined with a slit width of 25 μm provides a spectral dispersion of 2.7 cm^{-1}/pixel and allows for subpixel fitting of the Raman spectrum to within ±0.5 cm^{-1}. Owing to the optical transparency and high thermal conductivity of the SiC substrate, 18 mW of power could be utilized for the 532 nm investigations without damaging the graphene, as evidenced by the lack of D-peak in all acquired spectra (see Figure 1). By monitoring the G-mode peak position as a function of laser power on an analogous sample of epitaxial monolayer graphene, changes in the Raman spectrum due to laser heating were found to be smaller than the spectral resolution of the instrument for the conditions described above. Laser heating, therefore, did not impact the measurements.

Conflict of Interest: The authors declare no competing financial interest.

Acknowledgment. Special thanks to Jianyong Yang of WiTec Instruments GmBh for providing use of equipment and aid in the measurements presented herein. We are also grateful to R. Guild Copeland and Anthony McDonald for their respective efforts in the synthesis and characterization of these samples. This work was supported by the LDRD program at Sandia National Laboratories (SNL) and the U.S. DOE Office of Basic Energy Sciences (BES), Division of Materials Science and Engineering. Sandia National Laboratories is a multiprogram laboratory managed and operated by Sandia Corporation, a wholly owned subsidiary of Lockheed Martin Corporation, for the U.S. DOE National Nuclear Security Administration under Contract No. DE-AC04-94AL85000. The work at NRL was funded by the Office of Naval Research and NRL's NanoScience Institute.

REFERENCES AND NOTES

1. Novoselov, K.; Jiang, D.; Schedin, F.; Booth, T.; Khotkevich, V.; Morozov, S.; Geim, A. Two-Dimensional Atomic Crystals. *Proc. Natl. Acad. Sci. U.S.A.* **2005**, *102*, 10451–10453.
2. Wang, H.; Taychatanapat, T.; Hsu, A.; Watanabe, K.; Taniguchi, T.; Jarillo-Herrero, P.; Palacios, T. BN/Graphene/BN Transistors for RF Applications. *IEEE Electron Device Lett.* **2011**, *32*, 1209–1211.
3. Neto, A.; Novoselov, K. New Directions in Science and Technology: Two-Dimensional Crystals. *Rep. Prog. Phys.* **2011**, *74*, 82501–82509.
4. Butler, S. Z.; Hollen, S. M.; Cao, L.; Cui, Y.; Gupta, J. A.; Gutiérrez, H. R.; Heinz, T. F.; Hong, S. S.; Huang, J.; Ismach, A. F.; *et al.* Progress, Challenges, and Opportunities in Two-Dimensional Materials beyond Graphene. *ACS Nano* **2013**, *7*, 2898–2926.
5. Geim, A. K.; Grigorieva, I. V. Van der Waals Heterostructures. *Nature* **2013**, *499*, 419–425.
6. Robinson, J. T.; Schmucker, S. W.; Diaconescu, C. B.; Long, J. P.; Culbertson, J. C.; Ohta, T.; Friedman, A. L.; Beechem, T. E. Electronic Hybridization of Large-Area Stacked Graphene Films. *ACS Nano* **2012**, *7*, 637–644.
7. Wang, Y.; Ni, Z.; Liu, L.; Liu, Y.; Cong, C.; Yu, T.; Wang, X.; Shen, D.; Shen, Z. Stacking-Dependent Optical Conductivity of Bilayer Graphene. *ACS Nano* **2010**, *4*, 4074–4080.
8. Moon, P.; Koshino, M. Optical Absorption in Twisted Bilayer Graphene. *Phys. Rev. B* **2013**, *87*, 205404.
9. Yankowitz, M.; Xue, J.; Cormode, D.; Sanchez-Yamagishi, J. D.; Watanabe, K.; Taniguchi, T.; Jarillo-Herrero, P.; Jacquod, P.; LeRoy, B. J. Emergence of Superlattice Dirac Points in Graphene on Hexagonal Boron Nitride. *Nat. Phys.* **2012**, *8*, 382–386.
10. Ortix, C.; Yang, L.; van den Brink, J. Graphene on Incommensurate Substrates: Trigonal Warping and Emerging Dirac Cone Replicas with Halved Group Velocity. *Phys. Rev. B* **2012**, *86*, 081405.
11. Dean, C.; Wang, L.; Maher, P.; Forsythe, C.; Ghahari, F.; Gao, Y.; Katoch, J.; Ishigami, M.; Moon, P.; Koshino, M. Hofstadter's Butterfly and the Fractal Quantum Hall Effect in Moiré Superlattices. *Nature* **2013**, *497*, 598–602.
12. Hunt, B.; Sanchez-Yamagishi, J. D.; Young, A. F.; Yankowitz, M.; LeRoy, B. J.; Watanabe, K.; Taniguchi, T.; Moon, P.; Koshino, M.; Jarillo-Herrero, P.; *et al.* Massive Dirac Fermions and Hofstadter Butterfly in a van der Waals Heterostructure. *Science* **2013**, *340*, 1427–1430.
13. Ohta, T.; Robinson, J. T.; Feibelman, P. J.; Bostwick, A.; Rotenberg, E.; Beechem, T. E. Evidence for Interlayer Coupling and Moiré Periodic Potentials in Twisted Bilayer Graphene. *Phys. Rev. Lett.* **2012**, *109*, 186807.
14. Lopes dos Santos, J.; Peres, N.; Castro Neto, A. Graphene Bilayer with a Twist: Electronic Structure. *Phys. Rev. Lett.* **2007**, *99*, 256802.
15. Luican, A.; Li, G.; Reina, A.; Kong, J.; Nair, R.; Novoselov, K.; Geim, A.; Andrei, E. Single-Layer Behavior and Its Breakdown in Twisted Graphene Layers. *Phys. Rev. Lett.* **2011**, *106*, 126802.
16. Jiang, J.; Wang, B.; Rabczuk, T. Acoustic and Breathing Phonon Modes in Bilayer Graphene with Moiré Patterns. *Appl. Phys. Lett.* **2012**, *101*, 023113.
17. Zhang, J.; Zhao, J. Mechanical Properties of Bilayer Graphene with Twist and Grain Boundaries. *J. Appl. Phys.* **2013**, *113*, 043514.
18. Cocemasov, A. I.; Nika, D. L.; Balandin, A. A. Phonons in Twisted Bilayer Graphene. *Phys. Rev. B* **2013**, *88*, 035428.
19. Bistritzer, R.; MacDonald, A. Moiré Butterflies in Twisted Bilayer Graphene. *Phys. Rev. B* **2011**, *84*, 35440.

20. Righi, A.; Costa, S. D.; Chacham, H.; Fantini, C.; Venezuela, P.; Magnuson, C.; Colombo, L.; Bacsa, W. S.; Ruoff, R. S.; Pimenta, M. A. Graphene Moiré Patterns Observed by Umklapp Double-Resonance Raman Scattering. *Phys. Rev. B* **2011**, *84*, 241409.
21. Hass, J.; Varchon, F.; Millán-Otoya, J. E.; Sprinkle, M.; Sharma, N.; de Heer, W. A.; Berger, C.; First, P. N.; Magaud, L.; Conrad, E. H. Why Multilayer Graphene on 4H-SiC(0001) Behaves Like a Single Sheet of Graphene. *Phys. Rev. Lett.* **2008**, *100*, 125504.
22. Mele, E. J. Commensuration and Interlayer Coherence in Twisted Bilayer Graphene. *Phys. Rev. B* **2010**, *81*, 161405.
23. Mele, E. J. Band Symmetries and Singularities in Twisted Multilayer Graphene. *Phys. Rev. B* **2011**, *84*, 235439.
24. Bistritzer, R.; MacDonald, A. H. Moiré Bands in Twisted Double-Layer Graphene. *Proc. Natl. Acad. Sci. U.S.A.* **2011**, *108*, 12233–12237.
25. Trambly de Laissardiere, G.; Mayou, D.; Magaud, L. Localization of Dirac Electrons in Rotated Graphene Bilayers. *Nano Lett.* **2010**, *10*, 804–808.
26. Shallcross, S.; Sharma, S.; Pankratov, O. Quantum Interference at the Twist Boundary in Graphene. *Phys. Rev. Lett.* **2008**, *101*, 56803.
27. Shallcross, S.; Sharma, S.; Kandelaki, E.; Pankratov, O. A. Electronic Structure of Turbostratic Graphene. *Phys. Rev. B* **2010**, *81*, 165105.
28. Li, G.; Luican, A.; Dos Santos, J.; Neto, A.; Reina, A.; Kong, J.; Andrei, E. Observation of Van Hove Singularities in Twisted Graphene Layers. *Nat. Phys.* **2009**, *6*, 109–113.
29. Ni, Z.; Wang, Y.; Yu, T.; You, Y.; Shen, Z. Reduction of Fermi Velocity in Folded Graphene Observed by Resonance Raman Spectroscopy. *Phys. Rev. B* **2008**, *77*, 235403.
30. Ni, Z.; Liu, L.; Wang, Y.; Zheng, Z.; Li, L.-J.; Yu, T.; Shen, Z. G-Band Raman Double Resonance in Twisted Bilayer Graphene: Evidence of Band Splitting and Folding. *Phys. Rev. B* **2009**, *80*, 125404.
31. Ohta, T.; Beechem, T. E.; Robinson, J. T.; Kellogg, G. L. Long-Range Atomic Ordering and Variable Interlayer Interactions in Two Overlapping Graphene Lattices with Stacking Misorientations. *Phys. Rev. B* **2012**, *85*, 075415.
32. Jiang, J.-W.; Wang, B.-S.; Rabczuk, T. Why Twisting Angles Are Diverse in Graphene Moiré Patterns? *J. Appl. Phys.* **2013**, *113*, 194304.
33. Kim, K. S.; Walter, A. L.; Moreschini, L.; Seyller, T.; Horn, K.; Rotenberg, E.; Bostwick, A. Coexisting Massive and Massless Dirac Fermions in Symmetry-Broken Bilayer Graphene. *Nat. Mater.* **2013**, *12*, 887–892.
34. Nie, S.; Wofford, J.; Bartelt, N.; Dubon, O.; McCarty, K. Origin of the Mosaicity in Graphene Grown on Cu (111). *Phys. Rev. B* **2011**, *84*, 155425.
35. Jegal, S.; Hao, Y.; Yoon, D.; Ruoff, R. S.; Yun, H.; Lee, S. W.; Cheong, H. Crystallographic Orientation of Early Domains in CVD Graphene Studied by Raman Spectroscopy. *Chem. Phys. Lett.* **2013**, *568*−*569*, 146–150.
36. Li, X.; Magnuson, C. W.; Venugopal, A.; Tromp, R. M.; Hannon, J. B.; Vogel, E. M.; Colombo, L.; Ruoff, R. S. Large-Area Graphene Single Crystals Grown by Low-Pressure Chemical Vapor Deposition of Methane on Copper. *J. Am. Chem. Soc.* **2011**, *133*, 2816.
37. Robinson, J. A.; Puls, C. P.; Staley, N. E.; Stitt, J. P.; Fanton, M. A.; Emtsev, K. V.; Seyller, T.; Liu, Y. Raman Topography and Strain Uniformity of Large-Area Epitaxial Graphene. *Nano Lett.* **2009**, *9*, 964–968.
38. Schmidt, D.; Ohta, T.; Beechem, T. Strain and Charge Carrier Coupling in Epitaxial Graphene. *Phys. Rev. B* **2011**, *84*, 235422.
39. Havener, R. W.; Zhuang, H.; Brown, L.; Hennig, R. G.; Park, J. Angle-Resolved Raman Imaging of Interlayer Rotations and Interactions in Twisted Bilayer Graphene. *Nano Lett.* **2012**, *12*, 3162–3167.
40. Kim, K.; Coh, S.; Tan, L. Z.; Regan, W.; Yuk, J. M.; Chatterjee, E.; Crommie, M. F.; Cohen, M. L.; Louie, S. G.; Zettl, A. Raman Spectroscopy Study of Rotated Double-Layer Graphene: Misorientation-Angle Dependence of Electronic Structure. *Phys. Rev. Lett.* **2012**, *108*, 246103.
41. Coh, S.; Tan, L. Z.; Louie, S. G.; Cohen, M. L. Theory of the Raman Spectrum of the Rotated Double-Layer Graphene. *Phys. Rev. B* **2013**, *88*, 165431.
42. Chen, C.-F.; Park, C.-H.; Boudouris, B. W.; Horng, J.; Geng, B.; Girit, C.; Zettl, A.; Crommie, M. F.; Segalman, R. A.; Louie, S. G. Controlling Inelastic Light Scattering Quantum Pathways in Graphene. *Nature* **2011**, *471*, 617–620.
43. Tabert, C. J.; Nicol, E. J. Optical Conductivity of Twisted Bilayer Graphene. *Phys. Rev. B* **2013**, *87*, 121402.
44. Das, A.; Pisana, S.; Chakraborty, B.; Piscanec, S.; Saha, S.; Waghmare, U.; Novoselov, K.; Krishnamurthy, H.; Geim, A.; Ferrari, A. Monitoring Dopants by Raman Scattering in an Electrochemically Top-Gated Graphene Transistor. *Nat. Nanotechnol.* **2008**, *3*, 210–215.
45. Mohiuddin, T.; Lombardo, A.; Nair, R.; Bonetti, A.; Savini, G.; Jalil, R.; Bonini, N.; Basko, D.; Galiotis, C.; Marzari, N. Uniaxial Strain in Graphene by Raman Spectroscopy: G Peak Splitting, Gruneisen Parameters, and Sample Orientation. *Phys. Rev. B* **2009**, *79*, 205433.
46. Haigh, S. J.; Gholinia, A.; Jalil, R.; Romani, S.; Britnell, L.; Elias, D. C.; Novoselov, K. S.; Ponomarenko, L. A.; Geim, A. K.; Gorbachev, R. Cross-Sectional Imaging of Individual Layers and Buried Interfaces of Graphene-Based Heterostructures and Superlattices. *Nat. Mater.* **2012**, *11*, 764–767.
47. Alden, J. S.; Tsen, A. W.; Huang, P. Y.; Hovden, R.; Brown, L.; Park, J.; Muller, D. A.; McEuen, P. L. Strain Solitons and Topological Defects in Bilayer Graphene. *Proc. Natl. Acad. Sci. U.S.A.* **2013**, *110*, 11256–11260.
48. Chen, C.-C.; Bao, W.; Theiss, J.; Dames, C.; Lau, C. N.; Cronin, S. B. Raman Spectroscopy of Ripple Formation in Suspended Graphene. *Nano Lett.* **2009**, *9*, 4172–4176.
49. Bao, W.; Miao, F.; Chen, Z.; Zhang, H.; Jang, W.; Dames, C.; Lau, C. N. Controlled Ripple Texturing of Suspended Graphene and Ultrathin Graphite Membranes. *Nat. Nanotechnol.* **2009**, *4*, 562–566.
50. Lee, J.; Ahn, G.; Shim, J.; Lee, Y.; Ryu, S. Optical Separation of Mechanical Strain from Charge Doping in Graphene. *Nat. Commun.* **2012**, *3*, 1024.
51. Sato, K.; Saito, R.; Cong, C.; Yu, T.; Dresselhaus, M. S. Zone Folding Effect in Raman G-Band Intensity of Twisted Bilayer Graphene. *Phys. Rev. B* **2012**, *86*, 125414.
52. Verhoeven, G.; Dienwiebel, M.; Frenken, J. Model Calculations of Superlubricity of Graphite. *Phys. Rev. B* **2004**, *70*, 165418.
53. Dienwiebel, M.; Verhoeven, G.; Pradeep, N.; Frenken, J.; Heimberg, J.; Zandbergen, H. Superlubricity of Graphite. *Phys. Rev. Lett.* **2004**, *92*, 126101.
54. Hod, O. Interlayer Commensurability and Superlubricity in Rigid Layered Materials. *Phys. Rev. B* **2012**, *86*, 075444.
55. Guo, Y.; Guo, W.; Chen, C. Modifying Atomic-Scale Friction between Two Graphene Sheets: A Molecular-Force-Field Study. *Phys. Rev. B* **2007**, *76*, 155429.
56. Brown, L.; Hovden, R.; Huang, P.; Wojcik, M.; Muller, D.; Park, J. Twinning and Twisting of Tri- and Bi-layer Graphene. *Nano Lett.* **2012**, *12*, 1609–1615.
57. Feng, X.; Kwon, S.; Park, J. Y.; Salmeron, M. Superlubric Sliding of Graphene Nanoflakes on Graphene. *ACS Nano* **2013**, *7*, 1718–1724.
58. Chu, Z.; He, W.; He, L. The Coexistence of van Hove Singularities and Superlattice Dirac Points in a Slightly Twisted Graphene Bilayer. *Phys. Rev. B* **2012**, *87*, 155419.
59. Lee, K.; Kim, S.; Points, M. S.; Beechem, T. E.; Ohta, T.; Tutuc, E. Magnetotransport Properties of Quasi-Free-Standing Epitaxial Graphene Bilayer on SiC: Evidence for Bernal Stacking. *Nano Lett.* **2011**, *11*, 3624–3628.
60. Feenstra, R.; Srivastava, N.; Gao, Q.; Widom, M.; Diaconescu, B.; Ohta, T.; Kellogg, G.; Robinson, J.; Vlassiouk, I. Low-Energy Electron Reflectivity from Graphene. *Phys. Rev. B* **2013**, *87*, 041406.